

# GaussHDR: High Dynamic Range Gaussian Splatting via Learning Unified 3D and 2D Local Tone Mapping

Jinfeng Liu<sup>1</sup> Lingtong Kong<sup>2</sup> Bo Li<sup>2</sup> Dan Xu<sup>1</sup>

<sup>1</sup>The Hong Kong University of Science and Technology <sup>2</sup>vivo Mobile Communication Co., Ltd

{jliugk,danxu}@cse.ust.hk, {ltkong,libra}@vivo.com

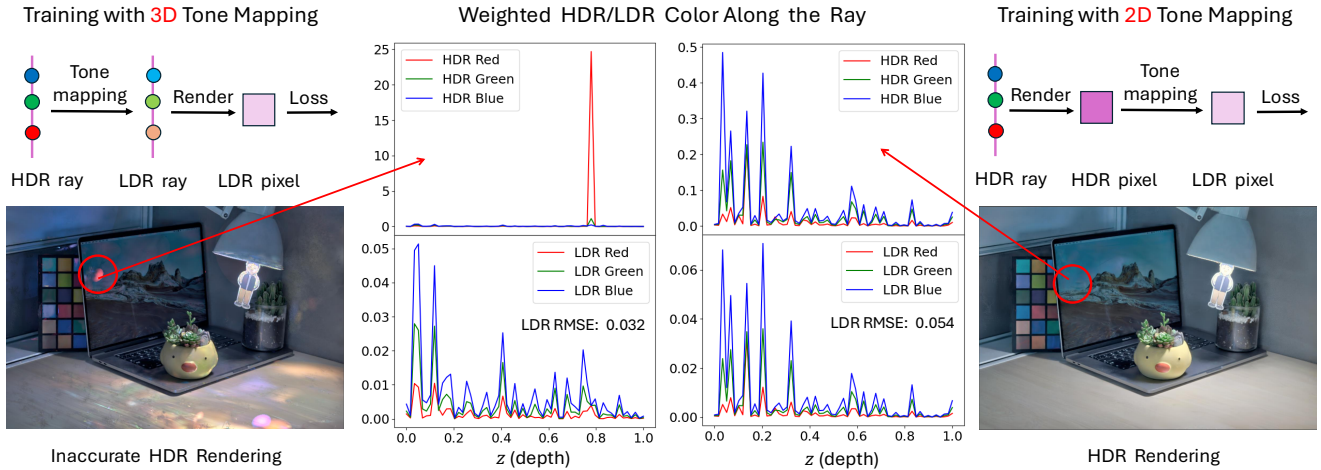


Figure 1. **3D tone mapping vs. 2D tone mapping.** Training with 3D tone mapping often results in inaccurate HDR rendering, while training with 2D tone mapping degrades LDR rendering quality, leading to a higher LDR RMSE metric compared to 3D tone mapping.

## Abstract

High dynamic range (HDR) novel view synthesis (NVS) aims to reconstruct HDR scenes by leveraging multi-view low dynamic range (LDR) images captured at different exposure levels. Current training paradigms with 3D tone mapping often result in unstable HDR reconstruction, while training with 2D tone mapping reduces the model’s capacity to fit LDR images. Additionally, the global tone mapper used in existing methods can impede the learning of both HDR and LDR representations. To address these challenges, we present GaussHDR, which unifies 3D and 2D local tone mapping through 3D Gaussian splatting. Specifically, we design a residual local tone mapper for both 3D and 2D tone mapping that accepts an additional context feature as input. We then propose combining the dual LDR rendering results from both 3D and 2D local tone mapping at the loss level. Finally, recognizing that different scenes may exhibit varying balances between the dual results, we introduce uncertainty learning and use the uncertainties for adaptive modulation. Extensive exper-

iments demonstrate that GaussHDR significantly outperforms state-of-the-art methods in both synthetic and real-world scenarios. The project page for this paper is available at <https://liujf1226.github.io/GaussHDR>.

## 1. Introduction

Nowadays, novel view synthesis (NVS) has reached an unprecedented level of advancement with the emergence of Neural Radiance Field (NeRF) [41] and 3D Gaussian Splatting (3DGS) [25], enabling realistic reconstruction and real-time rendering. This progress significantly benefits high dynamic range (HDR) NVS, which utilizes multi-view images captured at varying exposure levels to reconstruct HDR scenes. The objective is to render not only novel HDR views but also novel low dynamic range (LDR) views with controllable exposure. Currently, the mainstream paradigm for this task involves extending the color representation from LDR to HDR, and employing a tone mapper to model the camera response function (CRF), which maps the *exposure* (the product of HDR irradiance and camera exposure time)

into LDR color. Although methods [7, 18, 21, 59] based on this framework have demonstrated impressive results, the HDR and LDR fitting still faces severe challenges.

Considering the two LDR rendering methods illustrated in Fig. 1, training with 3D tone mapping tends to get stuck in HDR reconstruction while training with 2D tone mapping degrades LDR fitting ability. HDRGS [59] also points out the unstable HDR learning but attributes it to the MLP-based tone mapper. Here, we argue that this instability arises because 3D tone mapping separates HDR rendering from LDR supervision, which may lead to inconsistent HDR and LDR distributions along a ray, as depicted in the left part of Fig. 1. Consequently, training with 3D tone mapping is prone to converge to a local optimum where LDR fits well, but HDR fails. Employing 2D tone mapping can alleviate this problem (see the right part of Fig. 1) as LDR supervision is directly related to HDR rendering. However, the LDR results may deteriorate since HDR (from 0 to  $+\infty$ ) ray accumulation in 2D tone mapping is not as robust as standard LDR (from 0 to 1) ray accumulation. Thus, an intuitive idea is to make 3D and 2D tone mapping complement each other, thereby allowing our NVS system to render both HDR and LDR views with high quality. Nonetheless, the joint learning of 3D and 2D tone mapping is still constrained by the modeling capacity of the tone mapper.

Tone mapper serves as a bridge to connect HDR and LDR representations. The more accurately it can model real-world CRFs, the better HDR and LDR fitting will be. However, existing approaches [7, 18, 59] typically apply a *global* tone mapper across an entire scene. This makes a strong assumption that all 3D points or image pixels share the same tone-mapping characteristics, ignoring the fine-grained differences present at various spatial locations. In fact, local operators [3, 44, 63] in the field of HDR display have shown the ability to enhance visual details by adaptively processing pixels based on their positions.

To tackle the above-discussed problems, we present **GaussHDR**, a 3DGS-based method for HDR NVS, which unifies the learning of 3D and 2D local tone mapping. We choose 3DGS as the underlying representation because it provides comparable results to NeRFs while significantly improving the training and inference speeds. Building upon 3DGS, we first design a *residual local tone mapper* that is shared across the scene and can adapt to both 3D and 2D tone mapping. Unlike the global tone mapper, it accepts an additional feature vector as input to capture local characteristics. To this end, we assign each 3D Gaussian with a new attribute, *i.e.*, a context feature for 3D local tone mapping. The context features can be rendered from 3D Gaussians to 2D pixels in a manner similar to colors, resulting in a feature map for any given view. Consequently, each pixel will also possess its context feature for 2D local tone mapping. Then, we suggest combining the dual LDR rendering results

from 3D and 2D local tone mapping at the loss level to facilitate both HDR and LDR learning. Finally, different scenes may exhibit different balances between the dual results, we therefore introduce uncertainty learning for 3D and 2D local tone mapping and use the uncertainties to adaptively modulate their outcomes. Experiments on synthetic and real-world datasets demonstrate that our GaussHDR significantly surpasses state-of-the-art methods. The main contribution of this paper is summarized as follows:

- We present GaussHDR, a novel method that improves HDR Gaussian Splatting by unifying 3D and 2D local tone mapping, where we employ a residual local tone mapper to incorporate local spatial characteristics.
- We leverage the context feature assigned to each Gaussian as an additional input condition for the tone mapper in 3D local tone mapping. The context features are rendered concurrently with colors to ensure that each pixel possesses a context feature for 2D local tone mapping.
- We combine the dual LDR rendering results from 3D and 2D local tone mapping at the loss level and adaptively modulate them via uncertainty learning.

## 2. Related Works

**Novel View Synthesis.** NVS has experienced a significant breakthrough with the introduction of NeRF [41], which utilizes an MLP to implicitly model both the geometry and appearance of a scene. It leverages differentiable volume rendering [31], enabling training with a set of multi-view images. Follow-up NeRF variants aim to enhance its reconstruction quality [4, 5, 54] and efficiency [6, 9, 17, 43]. Despite these advancements, training and rendering speeds remain bottlenecks due to the dense sampling required in volume rendering. Recently, 3DGS [25] has emerged as a superior alternative to NeRF, which explicitly represents a scene by a set of 3D Gaussians. Thanks to the parallel rasterization (or splatting [65]) strategy, 3DGS is much more efficient than NeRFs while maintaining comparable rendering quality. Subsequent works have improved the functionality of 3DGS by incorporating anti-aliasing capabilities [34, 53, 62], applying depth regularization [12, 32] and reducing memory overhead [11, 15, 38, 56]. However, standard NVS methods only work on well-exposed LDR views and lack the capability to recover HDR scenes.

**High Dynamic Range Imaging.** Traditional HDR imaging approaches reconstruct HDR images by merging multi-exposure LDR images captured from a fixed viewpoint [40] or calibrating CRF from these images [13]. These methods often encounter motion artifacts when applied to dynamic environments. To mitigate this issue, later techniques propose estimating optical flow to detect motion regions in the LDR images, followed by removal [19] or alignment [22] during the fusion stage. Recent advancements in deep learning have led to the exploration of using CNNs [14, 27, 29]

and Transformers [10, 37, 52] to merge multi-exposure LDR images into a single HDR image. Nonetheless, most HDR imaging techniques require ground truth HDR images for supervision and cannot synthesize novel HDR views.

**High Dynamic Range Novel View Synthesis.** Existing HDR NVS methods can be classified into two main groups. The first group directly utilizes noisy RAW data [20, 33, 42, 51, 55], primarily for nighttime scenes. This paper focuses on the second group, which employs multi-exposure and multi-view LDR images for training [7, 18, 21, 58, 59]. Among them, HDR-NeRF [18] first proposes learning HDR radiance fields by predicting the HDR irradiance for each sampled point instead of the original LDR color. It also uses a tone mapper to convert the HDR irradiance into the LDR color. Subsequent methods, such as HDR-Plenoxels [21] and HDR-GS [7], aim to improve efficiency by replacing the NeRF representation with Plenoxels [16] and 3DGS, respectively. HDRGS [59] suggests employing an asymmetric gird-based tone mapper to enhance the reconstruction quality. HDR-HexPlane [58] extends this task to dynamic scenes using HexPlane [8] representation. However, 3D tone mapping in [7, 18] leads to unsteady HDR reconstruction while 2D tone mapping in [21, 59] harms LDR fitting. Besides, all these methods employ a global tone-mapper with a limited modeling capacity. In contrast, we combine 3D and 2D local tone mapping in this paper to facilitate both HDR and LDR learning.

### 3. The Proposed GaussHDR

#### 3.1. Preliminaries

**Gaussian Splatting.** 3DGS [25] utilizes a collection of anisotropic 3D neural Gaussians to model the scene. Each Gaussian possesses several attributes, including the position  $\mu \in \mathbb{R}^3$ , rotation quaternion  $r \in \mathbb{R}^4$ , scaling  $s \in \mathbb{R}^3$ , opacity  $\alpha \in [0, 1]$ , and color  $c \in \mathbb{R}^3$  (represented by spherical harmonics). With these properties, we can represent each Gaussian as  $G(x) = e^{-\frac{1}{2}(x-\mu)^T \Sigma^{-1}(x-\mu)}$ , where  $x$  is an arbitrary 3D position,  $\mu$  is Gaussian position (or mean), and  $\Sigma$  denotes the covariance matrix. To ensure the positive semi-definite property,  $\Sigma$  is decomposed as  $\Sigma = R S S^T R^T$ , where  $R$  is the rotation matrix derived from  $r$ , and  $S$  is the scaling matrix derived from  $s$ . Each 3D Gaussian  $G(x)$  is first transformed into a 2D Gaussian  $G'(x)$  on the image plane, as described in [65]. A tile-based rasterizer can then sort the 2D Gaussians and perform  $\alpha$ -blending:

$$C(p) = \sum_{i=1}^M c_i \sigma_i \prod_{j=1}^{i-1} (1 - \sigma_j), \quad \sigma_i = \alpha_i G'_i(p), \quad (1)$$

where  $p$  denotes the queried pixel position and  $M$  is the number of sorted 2D Gaussians related to the queried pixel.

**HDR Radiance Field.** To adapt the scene representation for HDR NVS, we replace the original LDR color attribute

$c \in [0, 1]$  with HDR irradiance  $e \in [0, +\infty)$ . Given the camera exposure time  $t$ , a tone mapper  $\phi$  is employed to model the camera response function (CRF) and map the HDR irradiance to LDR color as  $c = \phi(et)$ . Following previous works [7, 13, 18], we optimize the models in the logarithmic radiance domain to enhance training stability. Specifically, we can rewrite it as  $\ln \phi^{-1}(c) = \ln e + \ln t$ . Hence, our tone mapper can be transformed into a new function  $g = (\ln \phi^{-1})^{-1}$  such that:

$$c = g(\ln e + \ln t), \quad (2)$$

where we utilize three different tone mappers to model the RGB channels independently.

#### 3.2. GaussHDR

As discussed in Sec. 1, we aim to seamlessly integrate 3D tone mapping, which demonstrates excellent LDR fitting ability, with 2D tone mapping, which exhibits stable HDR reconstruction capacity, allowing them to complement each other. Besides, we seek to localize the tone mapper to model real-world CRFs more accurately. The key challenges are designing a local tone mapper applicable to both 3D and 2D tone mapping and effectively combining them. We present our solution GaussHDR. An overview is illustrated in Fig. 2. Firstly, Sec. 3.2.1 provides a brief formulation of the dual LDR rendering results under 3D and 2D tone mapping. Next, Sec. 3.2.2 and Sec. 3.2.3 explain how we localize the tone mapper for 3D and 2D local tone mapping. Finally, Sec. 3.2.4 introduces the uncertainty-based joint learning of 3D and 2D local tone mapping.

##### 3.2.1. Dual LDR Renderings

Given neural Gaussians with HDR irradiances  $\{e_i\}_{i=1}^N$  and a user-input exposure time  $t$ , we can transform them into LDR Gaussians  $\{c_i\}_{i=1}^N$  through 3D tone mapping:

$$c_i = g(\ln(e_i t)), \quad (3)$$

where  $g$  is the tone mapper in the logarithmic domain,  $i$  means the Gaussian index and  $N$  denotes the total number of Gaussians. We then render the LDR image  $I_{3d}$  at a given view from the LDR Gaussians:

$$I_{3d} = \mathcal{R}_P(\{c_i\}_{i=1}^N), \quad (4)$$

where  $\mathcal{R}_P$  denotes rasterization under camera pose  $P$ . For simplicity, we omit other auxiliary attributes here. Simultaneously, we can also render the HDR image  $E$  at the view from the HDR Gaussians:

$$E = \mathcal{R}_P(\{e_i\}_{i=1}^N), \quad (5)$$

which can be directly transformed into an LDR image  $I_{2d}$  using 2D tone mapping:

$$I_{2d} = g(\ln(Et)). \quad (6)$$

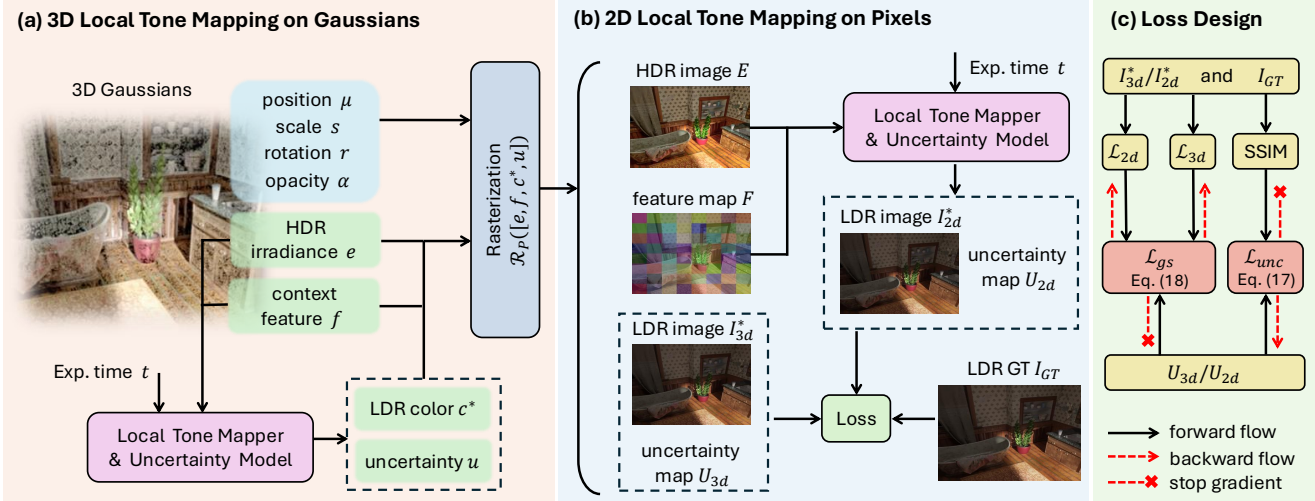


Figure 2. **Overview of the proposed GaussHDR.** (a) We assign each 3D Gaussian with a context feature for 3D local tone mapping and uncertainty prediction. HDR irradiance, context feature, LDR color and uncertainty are simultaneously rendered onto the image plane. (b) We perform 2D local tone mapping on the rendered HDR image and feature map and predict the uncertainty. (c) We combine the dual LDR rendering results under 3D and 2D local tone mapping at the loss level and utilize their uncertainties for adaptive modulation.

Now we have dual LDR rendering results for each view,  $I_{3d}$  and  $I_{2d}$ , under 3D and 2D tone mapping, respectively. Both can be used to calculate loss with ground truth but each has its inherent defects. Although the joint optimization of 3D and 2D tone mapping can combine their strengths, performance is still limited by current global tone mapper.

### 3.2.2. 3D and 2D Local Tone Mapping

Global tone mapper enforces the same tone-mapping characteristics across the scene, neglecting fine-grained spatial differences. Therefore, we propose to localize the tone mapper for both 3D and 2D tone mapping.

For 3D Gaussians, a direct way could be learning an individual set of tone-mapper parameters for each Gaussian according to its attributes, such as position. Nonetheless, this method is memory-intensive, as each tone mapper contains hundreds of parameters. Therefore, we consider incorporating local characteristics as input to the tone mapper rather than as parameters. For this purpose, MLP is more convenient than grid-based tone mappers [21, 59]. We can still employ a shared MLP across the scene which accepts the value  $\ln(e_it)$  along with some local attributes as input. A naive choice for local attributes could be the Gaussian position (or its Fourier encoding [41]). However, for image pixels, if we similarly use pixel positions as local attributes for tone mapping, we must also account for the distinctions between different views. In fact, HDR-Plenoxels [21] attempts to learn different global tone mappers for various training views, which can only fit existing views without generalization to unseen ones.

Fortunately, we notice that in language-embedded scene representation [26, 47, 50], the 3D and 2D language fea-

ture embeddings are connected through rendering. Pixel features rendered from Gaussian features exist in the same semantic space as Gaussian features. Inspired by this, we assign a new attribute to each Gaussian, *i.e.*, a context feature  $f \in \mathbb{R}^d$  for local tone mapping, where  $d$  is feature dimension. By rendering Gaussian features onto image plane, we can obtain a feature map  $F$  at the given view as follows:

$$F = \mathcal{R}_P(\{f_i\}_{i=1}^N), \quad (7)$$

which indicates that each pixel also corresponds to a context feature for tone mapping. Consequently, we can apply a shared tone mapper  $g^*$  to perform 3D local tone mapping:

$$I_{3d}^* = \mathcal{R}_P(\{c_i^*\}_{i=1}^N), \quad c_i^* = g^*(\ln(e_it), f_i), \quad (8)$$

and 2D local tone mapping:

$$I_{2d}^* = g^*(\ln(Et), F), \quad (9)$$

where  $c_i^*$  denotes the intermediate LDR color of the  $i$ -th Gaussian,  $I_{3d}^*$  and  $I_{2d}^*$  represent the dual LDR rendering results under 3D and 2D local tone mapping, respectively, as illustrated in Fig. 2(a-b).

### 3.2.3. Residual Local Tone Mapper

In this part, we describe the implementation of our local tone mapper  $g^*$ . To simplify the learning of  $g^*$ , we propose modeling it in a residual form. Concretely, we consider the global tone-mapping result as the primary component and add a residual term to incorporate local characteristics, as shown in Fig. 3. Consequently, local tone mapping can be expressed as:

$$c^* = g^*(\ln(et), f) = g(\ln(et)) + \Delta g([\ln(et), f]), \quad (10)$$

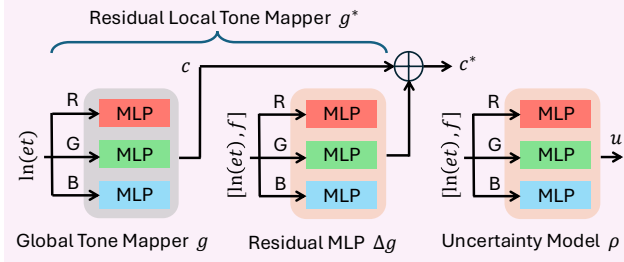


Figure 3. **Residual local tone mapper and uncertainty model.** We implement local tone mapper by adding a residual term to the global one. An uncertainty model is utilized to predict the uncertainty of local tone-mapping results.

where  $[\ ]$  means concatenation,  $g$  and  $\Delta g$  denote the global tone-mapping MLP and the residual MLP, respectively. In Eq. (10),  $c^*$  and  $e$  correspond to single-channel LDR and HDR colors, as we utilize three independent tone mappers for the RGB channels. The value of  $c^*$  is clipped to range  $[0, 1]$ . In this decomposition, the global tone-mapping MLP provides the foundational tonality while the residual MLP captures subtle local variations. By initially developing a well-fitted global tone mapper, we can more easily refine it with local adjustments. In practice, we disable the residual term during the first training stage, training solely with the global tone-mapping results. In the subsequent stage, we enable the residual MLP and optimize  $g$  and  $\Delta g$  simultaneously using the local tone-mapping results.

### 3.2.4. Joint Optimization via Uncertainty

To unify the learning of 3D and 2D local tone mapping, we try to combine the dual LDR rendering results  $I_{3d}^*$  and  $I_{2d}^*$ , at the loss level. Following 3DGS, we use a combination of DSSIM [57] and L1 losses to compute the image reconstruction error. Formally, given the LDR ground truth  $I_{GT}$ , the loss  $\mathcal{L}_{3d}$  on  $I_{3d}^*$  and loss  $\mathcal{L}_{2d}$  on  $I_{2d}^*$  can be calculated as:

$$\begin{aligned} \mathcal{L}_{3d} &= \lambda_d \text{DSSIM}(I_{3d}^*, I_{GT}) + (1 - \lambda_d) \|I_{3d}^* - I_{GT}\|_1, \\ \mathcal{L}_{2d} &= \lambda_d \text{DSSIM}(I_{2d}^*, I_{GT}) + (1 - \lambda_d) \|I_{2d}^* - I_{GT}\|_1. \end{aligned} \quad (11)$$

One can simply combine  $\mathcal{L}_{3d}$  and  $\mathcal{L}_{2d}$  through weighted summation. However, we observe that different scenes exhibit varying balances between these losses. To adapt GaussHDR for diverse scenarios, we introduce uncertainty learning [24] for both 3D and 2D local tone mapping.

**Uncertainty Learning.** We employ an uncertainty MLP, denoted as  $\rho$  in Fig. 3, to model the uncertainties of the dual LDR results  $I_{3d}^*$  and  $I_{2d}^*$ . This MLP also accepts  $\ln(et)$  and the context feature  $f$  as input, similar to the local tone mapper. Specifically, we predict the 3D tone-mapping uncertainties  $\{u_i\}_{i=1}^N$  for all Gaussians and render them onto the image plane to obtain the uncertainty map  $U_{3d}$  for  $I_{3d}^*$ , which is formulated as:

$$U_{3d} = \mathcal{R}_P(\{u_i\}_{i=1}^N), \quad u_i = \rho([\ln(et), f_i]). \quad (12)$$

The 2D tone-mapping uncertainty map  $U_{2d}$  for  $I_{2d}^*$  can also

be calculated similarly to Eq. (9), denoted as:

$$U_{2d} = \rho([\ln(et), F]). \quad (13)$$

Note that we clip the uncertainties with a minimal value of 0.1 [30, 48]. Subsequently, we use DSSIM, which causes more stable training dynamics compared to MSE [48], to optimize the uncertainties as follows:

$$\begin{aligned} \mathcal{L}_{3d\text{-unc}} &= \frac{\text{DSSIM}(I_{3d}^*, I_{GT})}{2U_{3d}^2} + \lambda_u \ln U_{3d}, \\ \mathcal{L}_{2d\text{-unc}} &= \frac{\text{DSSIM}(I_{2d}^*, I_{GT})}{2U_{2d}^2} + \lambda_u \ln U_{2d}, \end{aligned} \quad (14)$$

$$\mathcal{L}_{\text{unc}} = \mathcal{L}_{3d\text{-unc}} + \mathcal{L}_{2d\text{-unc}}.$$

**Joint Optimization.** Based on the learned uncertainties  $U_{3d}$  and  $U_{2d}$ , we can unify 3D and 2D local tone mapping within a joint learning framework, represented as:

$$\mathcal{L}_{\text{gs}} = \frac{U_{2d}^2 \mathcal{L}_{3d} + U_{3d}^2 \mathcal{L}_{2d}}{U_{3d}^2 + U_{2d}^2}, \quad (15)$$

where we utilize the uncertainties (or variances) to adaptively modulate  $\mathcal{L}_{3d}$  and  $\mathcal{L}_{2d}$ . Following [30, 39, 48], we separate the training of the 3DGS model from uncertainty prediction to ensure that the learned uncertainty is robust. By stopping gradients, as depicted in Fig. 2(c),  $\mathcal{L}_{\text{unc}}$  influences only the uncertainty predictor, while  $\mathcal{L}_{\text{gs}}$  affects only the 3DGS model and the tone mapper. Besides, for synthetic datasets, we follow HDR-NeRF [18] to incorporate a unit exposure loss on the global tone mapper  $g$  to fix the scale of learned HDR values, enabling HDR quality evaluation, denoted as  $\mathcal{L}_e = \|g(0) - 0.73\|_2^2$ . Therefore, the overall loss function for GaussHDR can be expressed as:

$$\mathcal{L} = \mathcal{L}_{\text{gs}} + \mathcal{L}_{\text{unc}} + \lambda_e \mathcal{L}_e. \quad (16)$$

When synthesizing LDR views after training, we can also leverage the uncertainties to merge the dual LDR results:

$$I_{\text{merge}} = \frac{U_{2d}^2 I_{3d}^* + U_{3d}^2 I_{2d}^*}{U_{3d}^2 + U_{2d}^2}, \quad (17)$$

where  $I_{\text{merge}}$  represents the merged LDR rendering, which is more robust than either of the dual results.

## 4. Experiments

### 4.1. Experimental Settings

**Datasets.** We utilize the multi-view and multi-exposure image datasets provided by HDR-NeRF [18], including 8 synthetic scenes created in Blender [1] and 4 real scenes captured with digital cameras. Each dataset contains 35 different views, each with 5 distinct exposure times  $\{t_1, t_2, t_3, t_4, t_5\}$ . The synthetic scenes also include HDR

Table 1. Quantitative comparisons on HDR-NeRF [18] and HDR-Plenoxels [21] real datasets. Metrics are averaged over all scenes. LDR-OE and LDR-NE denote the LDR results with exposure  $\{t_1, t_3, t_5\}$  and  $\{t_2, t_4\}$ , respectively. The training exposure setting is Exp-3.

Method	HDR-NeRF [18] Real Scenes						HDR-Plenoxels [21] Real Scenes					
	LDR-OE ( $t_1, t_3, t_5$ )			LDR-NE ( $t_2, t_4$ )			LDR-OE ( $t_1, t_3, t_5$ )			LDR-NE ( $t_2, t_4$ )		
	PSNR $\uparrow$	SSIM $\uparrow$	LPIPS $\downarrow$	PSNR $\uparrow$	SSIM $\uparrow$	LPIPS $\downarrow$	PSNR $\uparrow$	SSIM $\uparrow$	LPIPS $\downarrow$	PSNR $\uparrow$	SSIM $\uparrow$	LPIPS $\downarrow$
HDR-NeRF [18] †	34.31	0.954	0.062	32.29	0.949	0.071	-	-	-	-	-	-
HDR-GS [7]	35.47	0.970	0.022	31.66	0.965	0.030	-	-	-	-	-	-
HDR-GS [7] †	35.22	0.971	0.021	31.82	0.966	0.028	31.04	0.950	0.041	25.98	0.907	0.068
<b>Ours (3DGS)</b>	35.78	9.973	0.016	33.33	0.969	0.018	31.51	0.953	0.038	28.86	0.934	0.046
HDR-Scaffold-GS [38] *	35.96	0.975	0.013	32.66	0.971	0.016	32.12	0.955	0.032	29.17	0.935	0.040
<b>Ours (Scaffold-GS)</b>	<b>36.77</b>	<b>0.977</b>	<b>0.011</b>	<b>33.92</b>	<b>0.974</b>	<b>0.014</b>	<b>32.85</b>	<b>0.959</b>	<b>0.028</b>	<b>29.72</b>	<b>0.939</b>	<b>0.037</b>

† We re-implement HDR-NeRF [18] and HDR-GS [7] under the same setting (Exp-3) for fair comparison.

\* We replace the scene representation in HDR-GS from 3DGS [25] to Scaffold-GS [38] to establish a baseline for our method utilizing Scaffold-GS.

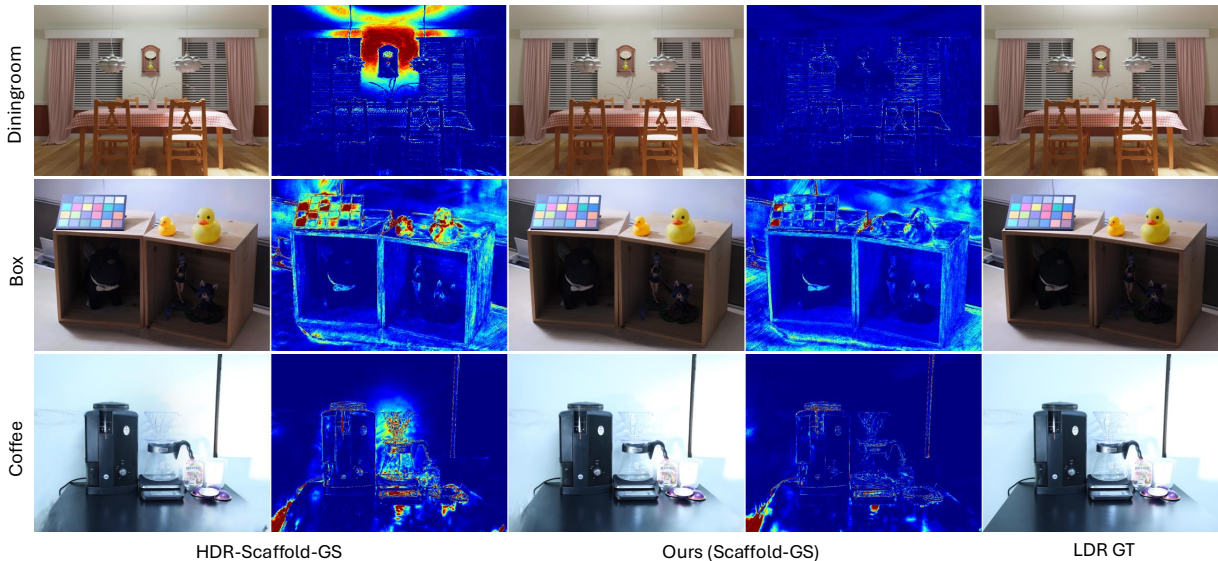


Figure 4. Qualitative LDR comparisons. Error maps in column 2 and 4 show the MSE error compared to the ground truth, where color from blue to red indicates the error from small to large. Our method can reduce LDR fitting errors in some regions.

ground truth (GT) for each view. For training, we use images from 18 views with exposure  $\{t_1, t_3, t_5\}$ . The remaining 17 views, with exposure  $\{t_1, t_3, t_5\}$  (LDR-OE) and  $\{t_2, t_4\}$  (LDR-NE), along with the HDR GTs of the synthetic datasets, are utilized for evaluation. Additionally, we experiment with another 4 real datasets collected by HDR-Plenoxels [21], which consist of 40 different views. We use 27 views for training and other 13 views for testing.

**Implementation Details.** We employ both 3DGS [25] and its feature-based variant, Scaffold-GS [38], to verify the effectiveness of the proposed GaussHDR. For Scaffold-GS, since it already provides a feature for each anchor point, we use a linear layer to project this feature into  $f \in \mathbb{R}^d$  for local tone mapping, where  $d$  is set to 4. The loss weights  $\lambda_d$ ,  $\lambda_u$ , and  $\lambda_e$  are set to 0.2, 0.5, and 0.5, respectively. All tone-mapper and uncertainty MLPs consist of one hidden layer with 64 channels. Similar to HDR-GS [7], we recalibrate the camera parameters and extract the initial point clouds for all scenes using COLMAP [49]. Models are trained for 30K iterations using the Adam [28] optimizer. During the

first 6K iterations, we disable the residual MLP and utilize global tone-mapping results for training. After that, we optimize the whole local tone mapper. All experiments are conducted using Pytorch [45] on a single RTX 3090 GPU. We experiment with two different training exposure settings. The first (Exp-1) strictly follows HDR-NeRF [18], which randomly selects one exposure from  $\{t_1, t_3, t_5\}$  for each view and keep it fixed during training. The second (Exp-3) aligns with HDR-GS [7], where we randomly select an exposure for the sampled view in each training iteration. Exp-1 means only one exposure is used for each view during training, while Exp-3 means all three exposures are accessible during training.

**Evaluation Metrics.** We employ PSNR (higher is better) and SSIM (higher is better) metrics, as well as LPIPS [64] (lower is better) perceptual metric for quantitative evaluation. Following HDR-NeRF [18], we quantitatively evaluate HDR results in the tone-mapped domain via the  $\mu$ -law [22] and qualitatively show HDR results tone-mapped by Photomatix pro [2].

Table 2. Quantitative comparisons on HDR-NeRF [18] synthetic datasets. Metrics are averaged over all scenes. LDR-OE and LDR-NE denote the LDR results with exposure  $\{t_1, t_3, t_5\}$  and  $\{t_2, t_4\}$ , respectively. HDR denotes the HDR results. The training setting is Exp-3.

Method	LDR-OE ( $t_1, t_3, t_5$ )			LDR-NE ( $t_2, t_4$ )			HDR		
	PSNR $\uparrow$	SSIM $\uparrow$	LPIPS $\downarrow$	PSNR $\uparrow$	SSIM $\uparrow$	LPIPS $\downarrow$	PSNR $\uparrow$	SSIM $\uparrow$	LPIPS $\downarrow$
HDR-NeRF [18] †	40.16	0.976	0.019	39.29	0.975	0.020	38.10	0.964	0.020
HDR-GS [7]	41.10	0.982	0.011	36.33	0.977	0.016	38.31	0.972	0.013
HDR-GS [7] †	41.13	0.983	0.009	39.78	0.980	0.012	26.98	0.901	0.042
<b>Ours (3DGS)</b>	42.29	0.985	0.007	41.57	0.985	0.007	37.62	0.971	0.016
HDR-Scaffold-GS [38] *	43.16	0.989	0.004	42.35	0.988	0.005	29.22	0.950	0.025
<b>Ours (Scaffold-GS)</b>	<b>43.78</b>	<b>0.990</b>	<b>0.003</b>	<b>43.00</b>	<b>0.990</b>	<b>0.004</b>	<b>39.02</b>	<b>0.976</b>	<b>0.010</b>

† We re-implement HDR-NeRF [18] and HDR-GS [7] under the same setting (Exp-3) for fair comparison. Note that the authors of HDR-GS utilize HDR ground truth (GT) for supervision during training on synthetic datasets, whereas our re-implementation does not include this supervision.

\* We replace the scene representation in HDR-GS from 3DGS [25] to Scaffold-GS [38] to establish a baseline for our method utilizing Scaffold-GS.



Figure 5. Qualitative HDR comparisons. Our method leads to stable HDR reconstruction results compared to HDR-Scaffold-GS baseline.



Figure 6. HDR visualization with residual design or not.

## 4.2. Performance Comparison

To establish a baseline for our method utilizing Scaffold-GS, we also conduct experiments with HDR-Scaffold-GS, which replaces the 3DGS representation in HDR-GS [7] with Scaffold-GS. In this part, we mainly compare under the Exp-3 setting. Comparison results under the Exp-1 setting are provided in the supplementary materials.

**Quantitative Comparison.** The quantitative results of real and synthetic datasets are listed in Tab. 1 and Tab. 2, respectively. It is evident that substituting 3DGS with Scaffold-GS results in improvements across all tracks. This can be attributed to the feature-based GS structure, which can better represent unbounded HDR colors compared to vanilla 3DGS employing spherical harmonics. Furthermore, regardless of whether using 3DGS or Scaffold-GS represen-

tations, our method consistently outperforms their corresponding baselines (HDR-GS and HDR-Scaffold-GS, respectively) by a substantial margin. Note that HDR-GS leverages HDR ground truth (GT) for supervision during training on synthetic datasets, resulting in strong HDR performance as shown in Tab. 2, whereas our implementation does not include this supervision. Nevertheless, our method, which integrates both 3D and 2D tone mapping, achieves comparable HDR results to HDR-GS. Overall, our GaussHDR demonstrates state-of-the-art performance across all tracks for both real and synthetic datasets.

**Qualitative Comparison.** We present visual comparison results for LDR and HDR NVS in Fig. 4 and Fig. 5, respectively. Clearly, our method reduces LDR fitting errors and enhances HDR reconstruction stability compared to the baseline, thereby facilitating both HDR and LDR learning.

## 4.3. Ablation Study

In this part, we conduct ablation study to dive into each component of GaussHDR. All ablation experiments are based on Scaffold-GS under the Exp-1 setting.

**Effect of 3D + 2D Local Tone Mapping.** First, by comparing (a) to (b) and (c) to (d) in Tab. 3, we can observe

Table 3. Ablation results on each component of the proposed GaussHDR. TM indicates tone mapping while Res. means the residual form of local tone mapper. All experiments are based on Scaffold-GS under the Exp-1 setting. All the metrics listed here represent PSNR.

	Method	LDR Test	HDR-NeRF [18] Real Scenes		HDR-NeRF [18] Synthetic Scenes		
			LDR-OE	LDR-NE	LDR-OE	LDR-NE	HDR
(a)	3D Global TM	$I_{3d}$	33.94	31.88	42.03	40.44	26.11
(b)	3D Local TM	$I_{3d}^*$	34.41	32.56	42.28	41.33	26.78
(c)	2D Global TM	$I_{2d}$	32.45	32.05	41.57	40.98	37.96
(d)	2D Local TM	$I_{2d}^*$	34.19	32.92	41.95	41.34	38.35
(e)	3D + 2D Global TM	$I_{merge}$	33.22	32.80	41.73	41.23	38.27
(f)	3D + 2D Local TM	$I_{3d}^*$	35.29	33.63	42.44	41.58	<b>38.60</b>
(g)	3D + 2D Local TM	$I_{2d}^*$	35.17	33.48	42.33	41.64	<b>38.60</b>
(h)	3D + 2D Local TM (w/o Res.)	$I_{merge}$	35.08	32.63	42.78	41.73	18.46
(i)	<b>3D + 2D Local TM (Ours)</b>	$I_{merge}$	<b>35.37</b>	<b>33.68</b>	<b>42.91</b>	<b>41.97</b>	<b>38.60</b>

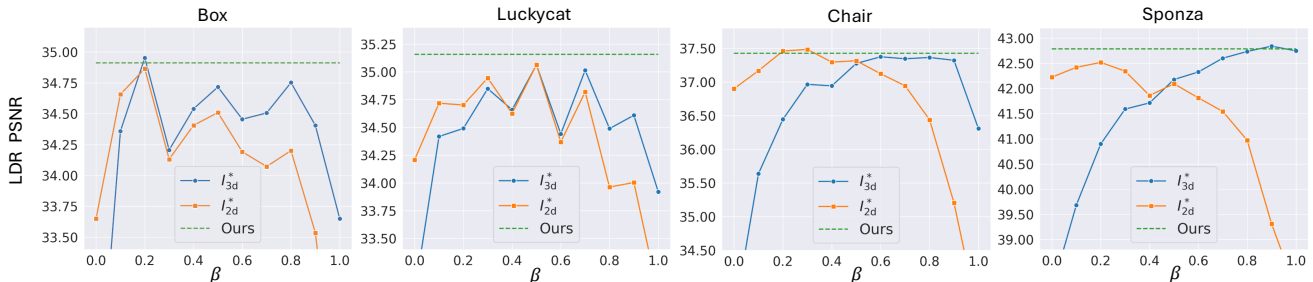


Figure 7. Performance variations of  $I_{3d}^*$  and  $I_{2d}^*$  with respect to  $\beta$  when simply using a loss combination  $\mathcal{L} = \beta\mathcal{L}_{3d} + (1 - \beta)\mathcal{L}_{2d}$ . Different scenes exhibit varying optimal values of  $\beta$ . In contrast, our uncertainty-based modulation (green dash line) can robustly achieve optimal results across diverse scenes without the selection of hyper-parameter  $\beta$ . The results of other scenes are in the supplementary materials.

the effectiveness of local tone mapping. No matter whether it is 3D or 2D global tone mapping, the local counterparts can consistently improve the performance. Another observation is that 3D tone mapping demonstrates poorer HDR performance but better LDR-OE fitting ability compared to 2D tone mapping, which has been discussed in Sec. 1. Furthermore, when unifying the learning of 3D and 2D local tone mapping through uncertainty, both LDR and HDR rendering quality can be further enhanced, as illustrated in Tab. 3(i). Additionally, we present the unified learning results under global tone mapping in Tab. 3(e), which exhibit inferior performance compared to (i), indicating that local tone mapping is crucial for the joint learning.

**Effect of Residual Local Tone Mapper.** To evaluate the effectiveness of the residual design in the local tone mapper, we experiment by utilizing the residual results as the local tone-mapping outcomes. As shown in Tab. 3(h), this approach causes a degradation in LDR performance, primarily due to the inherent difficulties in learning a local tone mapper without the benefit of initialization from a global tone mapper. Furthermore, HDR performance also deteriorates significantly, as illustrated in Fig. 6. This deterioration arises owing to the absence of direct HDR constraints from the global tone mapper. Consequently, the local tone mapper heavily relies on the context features, leading to overfitting in LDR and the collapse of HDR.

**Effect of Uncertainty Learning.** To investigate the role of

uncertainty in our unified learning framework (Eq. (15)), we perform experiments using a mixed loss function defined as  $\mathcal{L} = \beta\mathcal{L}_{3d} + (1 - \beta)\mathcal{L}_{2d}$ , which simply combines  $\mathcal{L}_{3d}$  and  $\mathcal{L}_{2d}$  through weighted summation. The performance variations of  $I_{3d}^*$  and  $I_{2d}^*$  with respect to the hyper-parameter  $\beta$  are depicted in Fig. 7, revealing that different scenes exhibit varying balances between 3D and 2D tone mapping. Notably, the uncertainty-based modulation in GaussHDR robustly achieves optimal results across diverse scenes. Moreover, our uncertainty-based merging of the dual LDR results enhances the fusion of their reliable regions, resulting in improved performance compared to either of them, particularly for synthetic scenes, as listed in Tab. 3(f,g,i).

## 5. Conclusion

In conclusion, we present a novel method, GaussHDR, that enhances HDR Gaussian Splatting by learning unified 3D and 2D local tone mapping. Specifically, we design a residual local tone mapper for both 3D and 2D tone mapping, which accepts an additional context feature as input. Each Gaussian is assigned a context feature for 3D local tone mapping, and the context features are rendered onto the image plane to ensure that each pixel has an associated context feature for 2D local tone mapping. We combine the dual LDR renderings from 3D and 2D local tone mapping at the loss level and introduce uncertainty learning to adaptively modulate the dual results.

## References

- [1] Blender. <https://www.blender.org/>. 5
- [2] Photomatix Pro 6. <https://www.hdrsoft.com/>. 6
- [3] Mathieu Aubry, Sylvain Paris, Samuel W Hasinoff, Jan Kautz, and Frédo Durand. Fast local laplacian filters: Theory and applications. *ACM TOG*, 33(5):1–14, 2014. 2
- [4] Jonathan T. Barron, Ben Mildenhall, Matthew Tancik, Peter Hedman, Ricardo Martin-Brualla, and Pratul P. Srinivasan. Mip-nerf: A multiscale representation for anti-aliasing neural radiance fields. In *ICCV*, pages 5835–5844, 2021. 2
- [5] Jonathan T. Barron, Ben Mildenhall, Dor Verbin, Pratul P. Srinivasan, and Peter Hedman. Mip-nerf 360: Unbounded anti-aliased neural radiance fields. In *CVPR*, pages 5460–5469, 2022. 2
- [6] Jonathan T. Barron, Ben Mildenhall, Dor Verbin, Pratul P. Srinivasan, and Peter Hedman. Zip-nerf: Anti-aliased grid-based neural radiance fields. In *ICCV*, pages 19640–19648, 2023. 2
- [7] Yuanhao Cai, Zihao Xiao, Yixun Liang, Yulun Zhang, Xiaokang Yang, Yaoyao Liu, and Alan Yuille. Hdr-gs: Efficient high dynamic range novel view synthesis at 1000x speed via gaussian splatting. In *NeurIPS*, 2024. 2, 3, 6, 7, 12, 13, 14
- [8] Ang Cao and Justin Johnson. Hexplane: A fast representation for dynamic scenes. In *CVPR*, pages 130–141, 2023. 3
- [9] Anpei Chen, Zexiang Xu, Andreas Geiger, Jingyi Yu, and Hao Su. Tensorf: Tensorial radiance fields. In *ECCV*, pages 333–350, 2022. 2
- [10] Rufeng Chen, Bolun Zheng, Hua Zhang, Quan Chen, Chenggang Yan, Gregory Slabaugh, and Shanxin Yuan. Improving dynamic hdr imaging with fusion transformer. In *AAAI*, pages 340–349, 2023. 3
- [11] Yihang Chen, Qianyi Wu, Weiyao Lin, Mehrtaash Harandi, and Jianfei Cai. Hac: Hash-grid assisted context for 3d gaussian splatting compression. In *ECCV*, 2024. 2
- [12] Jaeyoung Chung, Jeongtaek Oh, and Kyoung Mu Lee. Depth-regularized optimization for 3d gaussian splatting in few-shot images. In *CVPRW*, pages 811–820, 2024. 2
- [13] Paul E. Debevec and Jitendra Malik. Recovering high dynamic range radiance maps from photographs. In *SIGGRAPH*, pages 369–378, 1997. 2, 3
- [14] Gabriel Eilertsen, Joel Kronander, Gyorgy Denes, Rafał K. Mantiuk, and Jonas Unger. Hdr image reconstruction from a single exposure using deep cnns. *ACM TOG*, 36(6):1–15, 2017. 2
- [15] Zhiwen Fan, Kevin Wang, Kairun Wen, Zehao Zhu, Dejia Xu, and Zhangyang Wang. Lightgaussian: Unbounded 3d gaussian compression with 15x reduction and 200+ fps. In *NeurIPS*, 2024. 2
- [16] Sara Fridovich-Keil, Alex Yu, Matthew Tancik, Qinhong Chen, Benjamin Recht, and Angjoo Kanazawa. Plenoxels: Radiance fields without neural networks. In *CVPR*, pages 5491–5500, 2022. 3
- [17] Wenbo Hu, Yuling Wang, Lin Ma, Bangbang Yang, Lin Gao, and Xiao Liu. Tri-miprf: Tri-mip representation for efficient anti-aliasing neural radiance fields. In *ICCV*, pages 19717–19726, 2023. 2
- [18] Xin Huang, Qi Zhang, Ying Feng, Hongdong Li, Xuan Wang, and Qing Wang. Hdr-nerf: High dynamic range neural radiance fields. In *CVPR*, pages 18377–18387, 2022. 2, 3, 5, 6, 7, 8, 11, 12, 13, 14, 16
- [19] Katrien Jacobs, Celine Loscos, and Greg Ward. Automatic high-dynamic range image generation for dynamic scenes. *IEEE Computer Graphics and Applications*, 28(2):84–93, 2008. 2
- [20] Xin Jin, Pengyi Jiao, Zheng-Peng Duan, Xingchao Yang, Chun-Le Guo, Bo Ren, and Chongyi Li. Lighting every darkness with 3dgs: Fast training and real-time rendering for hdr view synthesis. *arXiv:2406.06216*, 2024. 3
- [21] Kim Jun-Seong, Kim Yu-Ji, Moon Ye-Bin, and Tae-Hyun Oh. Hdr-plenoxels: Self-calibrating high dynamic range radiance fields. In *ECCV*, pages 384–401, 2022. 2, 3, 4, 6, 11, 12, 13
- [22] Nima Khademi Kalantari and Ravi Ramamoorthi. Deep high dynamic range imaging of dynamic scenes. *ACM TOG*, 36(4):1–12, 2017. 2, 6
- [23] Bingxin Ke, Anton Obukhov, and Shengyu Huang. Repurposing diffusion-based image generators for monocular depth estimation. In *CVPR*, pages 9492–9502, 2024. 12
- [24] Alex Kendall and Yarin Gal. What uncertainties do we need in bayesian deep learning for computer vision? In *NeurIPS*, pages 5580–5590, 2017. 5
- [25] Bernhard Kerbl, Georgios Kopanas, Thomas Leimkühler, and George Drettakis. 3d gaussian splatting for real-time radiance field rendering. *ACM TOG*, 42(4):1–14, 2023. 1, 2, 3, 6, 7, 11, 12, 13, 14
- [26] Justin Kerr, Chung Min Kim, Ken Goldberg, Angjoo Kanazawa, and Matthew Tancik. Lrf: Language embedded radiance fields. In *CVPR*, pages 19729–19739, 2023. 4
- [27] Junghee Kim, Siyeong Lee, Weiyao Lin, Mehrtaash Harandi, and Suk-Ju Kang. End-to-end differentiable learning to hdr image synthesis for multi-exposure images. In *AAAI*, pages 1780–1788, 2021. 2
- [28] Diederik P Kingma and Jimmy Ba. Adam: A method for stochastic optimization. In *ICLR*, 2015. 6
- [29] Lingtong Kong, Bo Li, Yike Xiong, Hao Zhang, Hong Gu, and Jinwei Chen. Safnet: Selective alignment fusion network for efficient hdr imaging. In *ECCV*, 2024. 2
- [30] Jonas Kulhanek, Songyou Peng, Zuzana Kukelova, Marc Pollefeys, and Torsten Sattler. Wildgaussians: 3d gaussian splatting in the wild. In *NeurIPS*, 2024. 5
- [31] Marc Levoy. Efficient ray tracing of volume data. *ACM TOG*, 9(3):245–261, 1990. 2
- [32] Jiahe Li, Jiawei Zhang, Xiao Bai, Jin Zheng, Xin Ning, and Jun Zhou. Dngaussian: Optimizing sparse-view 3d gaussian radiance fields with global-local depth normalization. In *CVPR*, pages 20775–20785, 2024. 2
- [33] Zhihao Li, Yufei Wang, Alex Kot, and Bihan Wen. From chaos to clarity: 3dgs in the dark. *arXiv:2406.08300*, 2024. 3
- [34] Zhihao Liang, Qi Zhang, Wenbo Hu, Ying Feng, Lei Zhu, and Kui Jia. Analytic-splatting: Anti-aliased 3d gaussian splatting via analytic integration. In *ECCV*, 2024. 2

- [35] Jinfeng Liu, Lingtong Kong, Bo Li, Zerong Wang, Hong Gu, and Jinwei Chen. Mono-vifi: A unified learning framework for self-supervised single and multi-frame monocular depth estimation. In *ECCV*, pages 90–107, 2024. 12
- [36] Jinfeng Liu, Lingtong Kong, Jie Yang, and Wei Liu. Towards better data exploitation in self-supervised monocular depth estimation. *IEEE Robotics and Automation Letters*, 9(1):763–770, 2024. 12
- [37] Zhen Liu, Yinglong Wang, Bing Zeng, and Shuaicheng Liu. Ghost-free high dynamic range imaging with context-aware transformer. In *ECCV*, pages 344–360, 2022. 3
- [38] Tao Lu, Mulin Yu, Linning Xu, Yuanbo Xiangli, Limin Wang, and Dahua Lin. Scaffold-gs: Structured 3d gaussians for view-adaptive rendering. In *CVPR*, pages 20654–20664, 2024. 2, 6, 7, 11, 12, 13, 14
- [39] Ricardo Martin-Brualla, Noha Radwan, Mehdi S. M. Sajjadi, Jonathan T. Barron, Alexey Dosovitskiy, and Daniel Duckworth. Nerf in the wild: Neural radiance fields for unconstrained photo collections. In *CVPR*, pages 7206–7215, 2021. 5
- [40] Tom Mertens, Jan Kautz, and Frank Van Reeth. Exposure fusion. In *15th Pacific Conference on Computer Graphics and Applications (PG'07)*, pages 382–390, 2007. 2
- [41] Ben Mildenhall, Pratul P. Srinivasan, Matthew Tancik, Jonathan T. Barron, Ravi Ramamoorthi, and Ren Ng. Nerf: Representing scenes as neural radiance fields for view synthesis. In *ECCV*, pages 405–421, 2020. 1, 2, 4
- [42] Ben Mildenhall, Peter Hedman, Ricardo Martin-Brualla, Pratul P. Srinivasan, and Jonathan T. Barron. Nerf in the dark: High dynamic range view synthesis from noisy raw images. In *CVPR*, pages 16169–16178, 2022. 3
- [43] Thomas Müller, Alex Evans, Christoph Schied, and Alexander Keller. Instant neural graphics primitives with a multiresolution hash encoding. *ACM TOG*, 41(4):1–15, 2022. 2
- [44] Sylvain Paris, Samuel W Hasinoff, and Jan Kautz. Local laplacian filters: Edge-aware image processing with a laplacian pyramid. *ACM TOG*, 58(3):81–91, 2015. 2
- [45] Adam Paszke et al. Pytorch: An imperative style, high-performance deep learning library. In *NeurIPS*, pages 8026–8037, 2019. 6
- [46] Luigi Piccinelli, Yung-Hsu Yang, Christos Sakaridis, Mattia Segu, Siyuan Li, Luc Van Gool, and Fisher Yu. Unidepth: Universal monocular metric depth estimation. In *CVPR*, pages 10106–10116, 2024. 12
- [47] Minghan Qin, Wanhua Li, Jiawei Zhou, Haoqian Wang, and Hanspeter Pfister. Langsplat: 3d language gaussian splatting. In *CVPR*, pages 20051–20060, 2024. 4
- [48] Weining Ren, Zihan Zhu, Boyang Sun, Jiaqi Chen, Marc Pollefeys, and Songyou Peng. Nerf on-the-go: Exploiting uncertainty for distractor-free nerfs in the wild. In *CVPR*, pages 8931–8940, 2024. 5
- [49] Johannes L. Schönberger and Jan-Michael Frahm. Structure-from-motion revisited. In *CVPR*, pages 4104–4113, 2016. 6, 12
- [50] Jin-Chuan Shi, Miao Wang, Hao-Bin Duan, and Shao-Hua Guan. Language embedded 3d gaussians for open-vocabulary scene understanding. In *CVPR*, pages 5333–5343, 2024. 4
- [51] Shreyas Singh, Aryan Garg, and Kaushik Mitra. Hdrsplat: Gaussian splatting for high dynamic range 3d scene reconstruction from raw images. In *BMVC*, 2024. 3
- [52] Jou Won Song, Ye-In Park, Kyeongbo Kong, Jaeho Kwak, and Suk-Ju Kang. Selective transhdr: Transformer-based selective hdr imaging using ghost region mask. In *ECCV*, pages 288–304, 2022. 3
- [53] Xiaowei Song, Jv Zheng, Shiran Yuan, Huan ang Gao, Jingwei Zhao, Xiang He, Weihao Gu, and Hao Zhao. Sags: Scale-adaptive gaussian splatting for training-free anti-aliasing. *arXiv:2403.19615*, 2024. 2
- [54] Dor Verbin, Peter Hedman, Ben Mildenhall, Todd Zickler, Jonathan T. Barron, and Pratul P. Srinivasan. Ref-nerf: Structured view-dependent appearance for neural radiance fields. In *CVPR*, pages 5481–5490, 2022. 2
- [55] Chao Wang, Krzysztof Wolski, Bernhard Kerbl, Ana Serrano, Mojtaba Bermana, Hans-Peter Seidel, Karol Myszkowski, and Thomas Leimkühler. Cinematic gaussians: Real-time hdr radiance fields with depth of field. *arXiv:2406.07329*, 2024. 3
- [56] Yufei Wang, Zhihao Li, Lanqing Guo, Wenhan Yang, Alex C. Kot, and Bihan Wen. Contextgs: Compact 3d gaussian splatting with anchor level context model. In *NeurIPS*, 2024. 2
- [57] Zhou Wang, Alan C. Bovik, Hamid R. Sheikh, and Eero P. Simoncelli. Image quality assessment: From error visibility to structural similarity. *IEEE TIP*, 13(4):600–612, 2004. 5
- [58] Guanjun Wu, Taoran Yi, Jiemin Fang, Wenyu Liu, and Xinggang Wang. Fast high dynamic range radiance fields for dynamic scenes. In *3DV*, pages 862–872, 2024. 3
- [59] Jiahao Wu, Lu Xiao, Rui Peng, Kaiqiang Xiong, and Ronggang Wang. Hdrgs: High dynamic range gaussian splatting. *arXiv:2408.06543*, 2024. 2, 3, 4
- [60] Lihe Yang, Bingyi Kang, Zilong Huang, Xiaogang Xu, Jiashi Feng, and Hengshuang Zhao. Depth anything: Unleashing the power of large-scale unlabeled data. In *CVPR*, pages 10371–10381, 2024. 12
- [61] Wei Yin, Chi Zhang, Hao Chen, Zhipeng Cai, Gang Yu, Kaixuan Wang, Xiaozhi Chen, and Chunhua Shen. Metric3d: Towards zero-shot metric 3d prediction from a single image. In *ICCV*, pages 9009–9019, 2023. 12
- [62] Zehao Yu, Anpei Chen, Binbin Huang, Torsten Sattler, and Andreas Geiger. Mip-splatting: Alias-free 3d gaussian splatting. In *CVPR*, pages 19447–19456, 2024. 2
- [63] Feng Zhang, Qingbo Lu, Ming Tian, Zhiqiang Li, Bin Xu, Changxin Gao, and Nong Sang. Lookup table meets local laplacian filter: Pyramid reconstruction network for tone mapping. In *NeurIPS*, 2023. 2
- [64] Richard Zhang, Phillip Isola, Alexei A Efros, Eli Shechtman, and Oliver Wang. The unreasonable effectiveness of deep features as a perceptual metric. In *CVPR*, pages 586–595, 2018. 6
- [65] Matthias Zwicker, Hanspeter Pfister, Jeroen Van Baar, and Markus Gross. Ewa volume splatting. In *Proceedings Visualization, 2001. VIS '01.*, pages 29–538, 2001. 2, 3

# GaussHDR: High Dynamic Range Gaussian Splatting via Learning Unified 3D and 2D Local Tone Mapping

## Supplementary Material

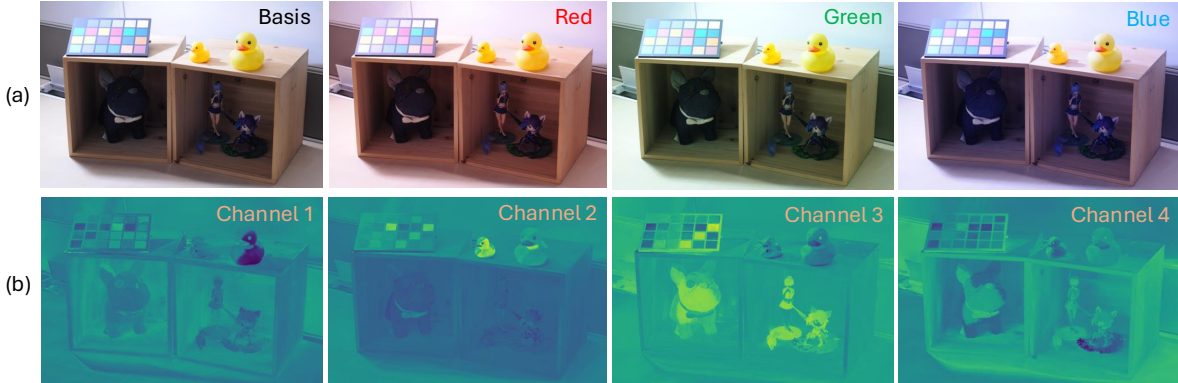


Figure 8. (a) By multiplying a factor to different RGB channels, we can control the white balance. (b) We visualize the 4-dimension context features channel by channel, which shows that different channels focus on capturing the tone-mapping characteristics of various regions.

## 6. Additional Implementation Details

**Datasets.** The original image resolutions of HDR-NeRF [18] synthetic and real datasets are  $800 \times 800$  and  $3216 \times 2136$ , respectively. We operate on the  $\frac{1}{2}$  scale for synthetic scenes, *i.e.*, a resolution of  $400 \times 400$ , and the  $\frac{1}{4}$  scale for real scenes, *i.e.*, a resolution of  $804 \times 534$ . For the four additional HDR-Plenoxels [21] real scenes, *desk* and *plant* scenes contain five different exposure times  $\{t_1, t_2, t_3, t_4, t_5\}$ , while *character* and *coffee* scenes include only three exposure times  $\{t_1, t_3, t_5\}$ . Consequently, we compute the averaged LDR-OE ( $t_1, t_3, t_5$ ) metrics across the four scenes and the averaged LDR-NE ( $t_2, t_4$ ) metrics over the *desk* and *plant* scenes. The original resolution of HDR-Plenoxels datasets is  $5952 \times 4480$ . We operate on the  $\frac{1}{6}$  scale, leading to a resolution of  $992 \times 746$ .

**Training Details.** When employing 3DGS [25] and Scaffold-GS [38] representations, we adhere to the same training parameters as those specified in [25] and [38], respectively. For our local tone mapper and uncertainty model, the learning rate is initially set to  $5 \times 10^{-4}$  and exponentially decays to  $5 \times 10^{-5}$ .

## 7. Additional Results

### 7.1. Performance Comparison

The HDR irradiance, tone mapper, and context features are coupled during the scene-specific optimization. However, once we have obtained the HDR radiance field, we can still control the white balance by multiplying a factor to different channels, as shown in Fig. 8(a). Similarly, we can ignore

the context features and switch to other known global tone mappers for different styles, since the context features are only applicable to the learned local tone mapper.

### 7.2. Performance Comparison

We have presented the quantitative comparison results under the Exp-3 setting in the main paper. Here, we provide the results under Exp-1 setting, which strictly follows HDR-NeRF [18] by randomly selecting one exposure from  $\{t_1, t_3, t_5\}$  for each view and keeping it fixed during training. The quantitative results for the real and synthetic datasets are listed in Tab. 5 and Tab. 6, respectively. Per-scene quantitative comparison outcomes are depicted in Tabs. 7 to 10. Additionally, we offer more examples of LDR and HDR qualitative results in the supplementary material, as demonstrated in Fig. 9 and Fig. 10, respectively. We also present three video demos corresponding to three different scenes: *bathroom* from HDR-NeRF [18] synthetic datasets, *flower* from HDR-NeRF real datasets, and *character* from HDR-Plenoxels [21] datasets. All the results further demonstrate that our method achieves state-of-the-art performance by improving both HDR and LDR learning.

### 7.3. Ablation on Uncertainty Learning

In the main paper, to investigate the effect of uncertainty learning, we perform experiments using a mixed loss function defined as  $\mathcal{L} = \beta \mathcal{L}_{3d} + (1 - \beta) \mathcal{L}_{2d}$ , which simply combines  $\mathcal{L}_{3d}$  and  $\mathcal{L}_{2d}$  through weighted summation. Then, we plot the performance variations of  $I_{3d}^*$  and  $I_{2d}^*$  with respect to the hyper-parameter  $\beta$ . Here, we show the results of more scenes, as depicted in Fig. 11, indicating that different

Table 4. Additional ablation results on HDR-NeRF[18] datasets. Pos. indicates using Gaussian position as context feature for local tone-mapping. LDR PSNR denotes the average metric over all 5 exposures. All experiments are under the Exp-1 setting.

	Method	HDR-NeRF [18] Real Scenes		HDR-NeRF [18] Synthetic Scenes	
		LDR PSNR		LDR PSNR	HDR PSNR
(a)	Ours-3DGS (with raw Pos.)	32.68		40.21	36.91
(b)	Ours-3DGS (with fourier-encoded Pos.)	32.95		40.63	37.09
(c)	Ours-3DGS	<b>33.58</b>		<b>41.32</b>	<b>37.41</b>
(d)	Ours-Scaffold-GS (direct learnable weights)	34.03		42.01	38.12
(e)	Ours-Scaffold-GS (3-layer MLPs, 128 nodes)	<b>34.75</b>		42.43	38.67
(f)	Ours-Scaffold-GS	34.69		<b>42.57</b>	<b>38.60</b>

Table 5. Quantitative comparisons on HDR-NeRF [18] and HDR-Plenoxels [21] real datasets. Metrics are averaged over all scenes. LDR-OE and LDR-NE denote the LDR results with exposure  $\{t_1, t_3, t_5\}$  and  $\{t_2, t_4\}$ , respectively. The training exposure setting is Exp-1.

Method	HDR-NeRF [18] Real Scenes						HDR-Plenoxels [21] Real Scenes					
	LDR-OE ( $t_1, t_3, t_5$ )			LDR-NE ( $t_2, t_4$ )			LDR-OE ( $t_1, t_3, t_5$ )			LDR-NE ( $t_2, t_4$ )		
	PSNR $\uparrow$	SSIM $\uparrow$	LPIPS $\downarrow$	PSNR $\uparrow$	SSIM $\uparrow$	LPIPS $\downarrow$	PSNR $\uparrow$	SSIM $\uparrow$	LPIPS $\downarrow$	PSNR $\uparrow$	SSIM $\uparrow$	LPIPS $\downarrow$
HDR-NeRF [18]	31.63	0.948	0.069	31.43	0.943	0.069	-	-	-	-	-	-
HDR-GS [7] †	33.56	0.964	0.024	31.18	0.960	0.027	30.18	0.943	0.044	27.63	0.916	0.056
<b>Ours (3DGS)</b>	34.18	0.965	0.019	32.63	0.962	0.021	30.99	0.947	0.041	28.08	0.923	0.050
HDR-Scaffold-GS [38] *	34.09	0.967	0.016	31.88	0.964	0.019	31.05	0.944	0.045	28.13	0.916	0.059
<b>Ours (Scaffold-GS)</b>	<b>35.37</b>	<b>0.972</b>	<b>0.014</b>	<b>33.68</b>	<b>0.969</b>	<b>0.016</b>	<b>32.24</b>	<b>0.954</b>	<b>0.031</b>	<b>28.98</b>	<b>0.932</b>	<b>0.041</b>

† We re-implement HDR-GS [7] under Exp-1 setting for fair comparison.

\* We replace the scene representation in HDR-GS from 3DGS [25] to Scaffold-GS [38] to establish a baseline for our method utilizing Scaffold-GS.

scenes exhibit varying balances between  $\mathcal{L}_{3d}$  and  $\mathcal{L}_{2d}$ . However, our uncertainty-based modulation can robustly achieve optimal results across diverse scenes.

Eq. (14) in the main paper can be viewed as a regularization term that encourages the model to learn meaningful uncertainties or variances. In this part, we also try to directly employ learnable weights for the dual LDR results without any regularization. As shown in Tab. 4(d), this approach results in a performance drop, again highlighting the effectiveness of our uncertainty modeling.

#### 7.4. Ablation on Tone-mapper MLPs

Since RGB channels may have different tone-mapping characteristics in real-world scenarios. Hence, using channel-specific MLPs for tone mapper is helpful, which has been verified in the HDR-NeRF [18] paper. Here, we also experiment with larger tone-mapper MLPs with deeper layers and more hidden nodes, as listed in Tab. 4(e). We can see that larger MLPs do not bring further improvements, but will increase the training and inference cost.

#### 7.5. Ablation on Context Feature

In the main paper, we claim that utilizing pixel positions in image space for 2D local tone mapping is infeasible, as we need to distinguish the same pixel position across different views. However, we can directly leverage Gaussian positions as tone-mapping context features and render them into image space. We conduct ablation experiments for this with 3DGS [25] representation, since Scaffold-GS [38] utilizes anchor context features to predict Gaussian positions. As listed in Tab. 4(a,b), it will cause a degraded performance

with either raw Gaussian positions or Fourier-encoded ones. Using Gaussian positions implies that various Gaussians that are far apart must possess distinct tone-mapping characteristics. However, in fact, different spatial locations may exhibit similar characteristics.

We also visualize the 4-dimension context feature channel by channel in Fig. 8(b), which indicates that different channels focus on capturing the tone-mapping characteristics of various regions.

## 8. Limitations

Despite the significant enhancements in HDR reconstruction and LDR fitting capabilities provided by GaussHDR, some limitations remain. First, our method relies on COLMAP [49] to extract the initial point cloud and compute camera poses. In other words, we must use tripod-mounted cameras to capture multi-exposure images at each sampled view. However, a more general application scenario could involve utilizing a hand-held camera to capture a monocular video around the scene, where each frame (or view) has a single exposure level, making it difficult to match images captured under different exposures in COLMAP. Therefore, a potential direction for future work is to develop a COLMAP-free version of GaussHDR. Second, it is promising to introduce depth priors to enhance geometry reconstruction by utilizing off-the-shelf depth models [23, 35, 36, 46, 60, 61]. Finally, our method focuses on static scenes and lacks the ability to perform HDR reconstruction in dynamic environments, which is also an area worth exploring.

Table 6. Quantitative comparisons on HDR-NeRF [18] synthetic datasets. Metrics are averaged over all scenes. LDR-OE and LDR-NE denote the LDR results with exposure  $\{t_1, t_3, t_5\}$  and  $\{t_2, t_4\}$ , respectively. HDR denotes the HDR results. The training setting is Exp-1.

Method	LDR-OE ( $t_1, t_3, t_5$ )			LDR-NE ( $t_2, t_4$ )			HDR		
	PSNR $\uparrow$	SSIM $\uparrow$	LPIPS $\downarrow$	PSNR $\uparrow$	SSIM $\uparrow$	LPIPS $\downarrow$	PSNR $\uparrow$	SSIM $\uparrow$	LPIPS $\downarrow$
HDR-NeRF [18]	39.07	0.973	0.026	37.53	0.966	0.024	36.40	0.936	0.018
HDR-GS [7] †	39.35	0.977	0.012	38.01	0.976	0.013	22.58	0.840	0.075
<b>Ours (3DGS)</b>	41.51	0.984	0.008	41.03	0.983	0.009	37.41	0.969	0.017
HDR-Scaffold-GS [38] *	42.21	0.986	0.005	40.44	0.986	0.006	26.11	0.915	0.062
<b>Ours (Scaffold-GS)</b>	<b>42.94</b>	<b>0.988</b>	<b>0.004</b>	<b>42.02</b>	<b>0.988</b>	<b>0.005</b>	<b>38.60</b>	<b>0.975</b>	<b>0.011</b>

† We re-implement HDR-GS [7] under Exp-1 setting for fair comparison. Note that the authors of HDR-GS utilize HDR ground truth (GT) for supervision during training on synthetic datasets, whereas our re-implementation does not include this supervision.

\* We replace the scene representation in HDR-GS from 3DGS [25] to Scaffold-GS [38] to establish a baseline for our method utilizing Scaffold-GS.

Table 7. Per-scene quantitative comparisons on HDR-NeRF [18] real datasets. LDR-OE and LDR-NE denote the LDR results with exposure  $\{t_1, t_3, t_5\}$  and  $\{t_2, t_4\}$ , respectively. The training exposure setting is Exp-1.

	Method	Box			Computer			Flower			Luckycat		
		PSNR $\uparrow$	SSIM $\uparrow$	LPIPS $\downarrow$	PSNR $\uparrow$	SSIM $\uparrow$	LPIPS $\downarrow$	PSNR $\uparrow$	SSIM $\uparrow$	LPIPS $\downarrow$	PSNR $\uparrow$	SSIM $\uparrow$	LPIPS $\downarrow$
LDR-OE	HDR-NeRF [18]	31.54	0.953	0.068	32.42	0.950	0.077	29.81	0.948	0.069	32.85	0.938	0.062
	HDR-GS [7] †	34.39	0.973	0.016	34.41	0.967	0.020	31.62	0.956	0.037	33.82	0.961	0.022
	<b>Ours (3DGS)</b>	35.87	0.976	0.012	34.99	0.967	0.020	31.84	0.958	0.024	34.03	0.961	0.020
	HDR-Scaffold-GS [38] *	34.66	0.974	0.012	34.55	0.965	0.017	32.70	0.967	0.019	34.43	0.963	0.016
	<b>Ours (Scaffold-GS)</b>	<b>36.24</b>	<b>0.979</b>	<b>0.010</b>	<b>35.50</b>	<b>0.970</b>	<b>0.015</b>	<b>34.12</b>	<b>0.971</b>	<b>0.014</b>	<b>35.61</b>	<b>0.970</b>	<b>0.015</b>
LDR-NE	HDR-NeRF [18]	31.40	0.944	0.079	31.21	0.931	0.098	30.05	0.949	0.058	33.13	0.948	0.051
	HDR-GS [7] †	30.17	0.967	0.021	32.78	0.966	0.023	30.21	0.954	0.039	31.55	0.954	0.026
	<b>Ours (3DGS)</b>	32.57	0.972	0.014	34.18	0.966	0.022	30.52	0.956	0.027	33.24	0.956	0.022
	HDR-Scaffold-GS [38] *	31.87	0.970	0.015	33.16	0.964	0.019	30.68	0.964	0.021	31.80	0.957	0.019
	<b>Ours (Scaffold-GS)</b>	<b>32.93</b>	<b>0.974</b>	<b>0.013</b>	<b>34.95</b>	<b>0.968</b>	<b>0.017</b>	<b>32.35</b>	<b>0.970</b>	<b>0.016</b>	<b>34.48</b>	<b>0.965</b>	<b>0.016</b>

† We re-implement HDR-GS [7] under Exp-1 setting for fair comparison.

\* We replace the scene representation in HDR-GS from 3DGS [25] to Scaffold-GS [38] to establish a baseline for our method utilizing Scaffold-GS.

Table 8. Per-scene quantitative comparisons on HDR-Plenoxels [21] real datasets. LDR-OE and LDR-NE denote the LDR results with exposure  $\{t_1, t_3, t_5\}$  and  $\{t_2, t_4\}$ , respectively. The training exposure setting is Exp-1.

	Method	Character			Coffee			Desk			Plant		
		PSNR $\uparrow$	SSIM $\uparrow$	LPIPS $\downarrow$	PSNR $\uparrow$	SSIM $\uparrow$	LPIPS $\downarrow$	PSNR $\uparrow$	SSIM $\uparrow$	LPIPS $\downarrow$	PSNR $\uparrow$	SSIM $\uparrow$	LPIPS $\downarrow$
LDR-OE	HDR-GS [7] †	34.96	0.978	0.027	27.79	0.943	0.049	28.78	0.922	0.045	29.18	0.930	0.054
	<b>Ours (3DGS)</b>	36.73	0.980	0.025	28.35	0.947	0.046	29.14	0.925	0.041	29.76	0.934	0.051
	HDR-Scaffold-GS [38] *	36.81	0.979	0.029	28.31	0.946	0.043	28.64	0.919	0.049	30.44	0.930	0.059
	<b>Ours (Scaffold-GS)</b>	<b>38.24</b>	<b>0.983</b>	<b>0.018</b>	<b>29.31</b>	<b>0.955</b>	<b>0.032</b>	<b>29.91</b>	<b>0.933</b>	<b>0.035</b>	<b>31.48</b>	<b>0.945</b>	<b>0.040</b>
LDR-NE	HDR-GS [7] †	-	-	-	-	-	-	27.08	0.912	0.050	28.17	0.920	0.061
	<b>Ours (3DGS)</b>	-	-	-	-	-	-	27.30	0.917	0.044	28.85	0.929	0.055
	HDR-Scaffold-GS [38] *	-	-	-	-	-	-	27.03	0.911	0.053	29.23	0.920	0.065
	<b>Ours (Scaffold-GS)</b>	-	-	-	-	-	-	<b>27.41</b>	<b>0.922</b>	<b>0.038</b>	<b>30.55</b>	<b>0.941</b>	<b>0.044</b>

† We re-implement HDR-GS [7] under Exp-1 setting for fair comparison.

\* We replace the scene representation in HDR-GS from 3DGS [25] to Scaffold-GS [38] to establish a baseline for our method utilizing Scaffold-GS.

Table 9. Per-scene quantitative comparisons on HDR-NeRF [18] synthetic datasets (Part 1). LDR-OE and LDR-NE denote the LDR results with exposure  $\{t_1, t_3, t_5\}$  and  $\{t_2, t_4\}$ , respectively. HDR denotes the HDR results. The training exposure setting is Exp-1.

	Method	Bathroom			Bear			Chair			Diningroom		
		PSNR $\uparrow$	SSIM $\uparrow$	LPIPS $\downarrow$	PSNR $\uparrow$	SSIM $\uparrow$	LPIPS $\downarrow$	PSNR $\uparrow$	SSIM $\uparrow$	LPIPS $\downarrow$	PSNR $\uparrow$	SSIM $\uparrow$	LPIPS $\downarrow$
LDR-OE	HDR-NeRF [18]	36.26	0.949	0.037	42.91	0.990	0.010	32.45	0.905	0.081	41.23	0.986	0.010
	HDR-GS [7] †	38.06	0.963	0.020	41.61	0.989	0.005	35.07	0.952	0.024	38.26	0.979	0.014
	<b>Ours (3DGS)</b>	41.12	0.975	0.008	44.44	0.992	0.003	37.05	0.968	0.014	39.63	0.981	0.017
	HDR-Scaffold-GS [38] *	41.21	0.977	0.008	44.56	0.992	0.003	36.36	0.966	0.016	44.87	<b>0.994</b>	<b>0.002</b>
	<b>Ours (Scaffold-GS)</b>	<b>42.08</b>	<b>0.981</b>	<b>0.006</b>	<b>45.40</b>	<b>0.993</b>	<b>0.002</b>	<b>37.65</b>	<b>0.971</b>	<b>0.012</b>	<b>45.21</b>	<b>0.994</b>	<b>0.002</b>
LDR-NE	HDR-NeRF [18]	33.44	0.926	0.046	41.19	0.987	0.012	30.78	0.886	0.083	37.99	0.979	0.013
	HDR-GS [7] †	36.03	0.963	0.024	41.69	0.988	0.005	34.05	0.951	0.026	34.62	0.976	0.020
	<b>Ours (3DGS)</b>	41.10	0.977	0.008	43.85	0.992	0.003	36.53	0.967	0.015	38.78	0.980	0.021
	HDR-Scaffold-GS [38] *	40.61	0.979	0.008	42.10	0.992	0.004	35.89	0.965	0.017	41.00	<b>0.993</b>	<b>0.003</b>
	<b>Ours (Scaffold-GS)</b>	<b>41.71</b>	<b>0.982</b>	<b>0.007</b>	<b>44.43</b>	<b>0.993</b>	<b>0.002</b>	<b>37.14</b>	<b>0.970</b>	<b>0.013</b>	<b>43.33</b>	<b>0.993</b>	<b>0.003</b>
HDR	HDR-NeRF [18]	33.97	0.925	0.048	<b>43.22</b>	<b>0.991</b>	0.008	34.14	0.924	0.069	38.57	0.981	0.015
	HDR-GS [7] †	15.48	0.739	0.125	30.99	0.961	0.027	20.47	0.751	0.115	18.86	0.860	0.074
	<b>Ours (3DGS)</b>	34.87	0.943	0.024	41.47	0.987	0.007	36.75	0.961	0.019	34.82	0.967	0.028
	HDR-Scaffold-GS [38] *	22.28	0.873	0.061	29.79	0.970	0.021	24.27	0.842	0.163	26.60	0.952	0.037
	<b>Ours (Scaffold-GS)</b>	<b>36.22</b>	<b>0.952</b>	<b>0.017</b>	42.23	0.988	<b>0.005</b>	<b>37.79</b>	<b>0.966</b>	<b>0.017</b>	<b>38.61</b>	<b>0.983</b>	<b>0.007</b>

† We re-implement HDR-GS [7] under Exp-1 setting for fair comparison.

\* We replace the scene representation in HDR-GS from 3DGS [25] to Scaffold-GS [38] to establish a baseline for our method utilizing Scaffold-GS.

Table 10. Per-scene quantitative comparisons on HDR-NeRF [18] synthetic datasets (Part 2). LDR-OE and LDR-NE denote the LDR results with exposure  $\{t_1, t_3, t_5\}$  and  $\{t_2, t_4\}$ , respectively. HDR denotes the HDR results. The training exposure setting is Exp-1.

	Method	Dog			Desk			Sofa			Sponza		
		PSNR $\uparrow$	SSIM $\uparrow$	LPIPS $\downarrow$	PSNR $\uparrow$	SSIM $\uparrow$	LPIPS $\downarrow$	PSNR $\uparrow$	SSIM $\uparrow$	LPIPS $\downarrow$	PSNR $\uparrow$	SSIM $\uparrow$	LPIPS $\downarrow$
LDR-OE	HDR-NeRF [18]	37.77	0.981	0.016	37.84	0.972	0.023	38.29	0.977	0.014	34.49	0.958	0.034
	HDR-GS [7] †	42.28	0.991	0.004	39.81	0.980	0.007	41.75	0.989	0.004	37.99	0.972	0.016
	<b>Ours (3DGS)</b>	43.06	0.992	0.004	42.28	0.987	0.004	43.04	0.990	<b>0.003</b>	41.43	0.986	0.007
	HDR-Scaffold-GS [38] *	43.31	0.993	0.003	41.72	0.987	0.004	43.26	<b>0.992</b>	<b>0.003</b>	42.43	0.990	<b>0.004</b>
	<b>Ours (Scaffold-GS)</b>	<b>43.76</b>	<b>0.994</b>	<b>0.002</b>	<b>43.04</b>	<b>0.990</b>	<b>0.003</b>	<b>43.44</b>	<b>0.992</b>	<b>0.003</b>	<b>42.91</b>	<b>0.991</b>	<b>0.004</b>
LDR-NE	HDR-NeRF [18]	36.52	0.976	0.018	35.26	0.960	0.029	38.35	0.976	0.014	33.41	0.950	0.038
	HDR-GS [7] †	40.66	0.990	0.004	38.47	0.980	0.007	41.55	0.989	0.004	36.99	0.975	0.015
	<b>Ours (3DGS)</b>	<b>42.24</b>	0.991	0.004	42.12	0.987	0.004	<b>42.34</b>	0.991	<b>0.003</b>	41.25	0.988	0.006
	HDR-Scaffold-GS [38] *	40.52	0.992	0.004	40.46	0.987	0.004	41.91	0.991	0.004	41.02	0.990	0.004
	<b>Ours (Scaffold-GS)</b>	42.12	<b>0.993</b>	<b>0.003</b>	<b>42.76</b>	<b>0.989</b>	<b>0.003</b>	42.03	<b>0.992</b>	<b>0.003</b>	<b>42.60</b>	<b>0.992</b>	<b>0.003</b>
HDR	HDR-NeRF [18]	<b>37.72</b>	<b>0.980</b>	0.016	43.38	<b>0.993</b>	0.007	<b>39.05</b>	<b>0.976</b>	0.017	32.33	0.939	0.049
	HDR-GS [7] †	23.02	0.926	0.037	29.11	0.773	0.082	26.60	0.928	0.046	16.12	0.782	0.095
	<b>Ours (3DGS)</b>	36.36	0.973	0.016	<b>43.98</b>	<b>0.993</b>	0.006	36.70	0.966	0.016	34.32	0.964	0.023
	HDR-Scaffold-GS [38] *	24.33	0.934	0.040	31.40	0.929	0.044	28.42	0.947	0.032	21.81	0.870	0.095
	<b>Ours (Scaffold-GS)</b>	37.52	0.978	<b>0.012</b>	43.83	<b>0.993</b>	<b>0.005</b>	36.99	0.969	<b>0.013</b>	<b>35.64</b>	<b>0.972</b>	<b>0.014</b>

† We re-implement HDR-GS [7] under Exp-1 setting for fair comparison.

\* We replace the scene representation in HDR-GS from 3DGS [25] to Scaffold-GS [38] to establish a baseline for our method utilizing Scaffold-GS.

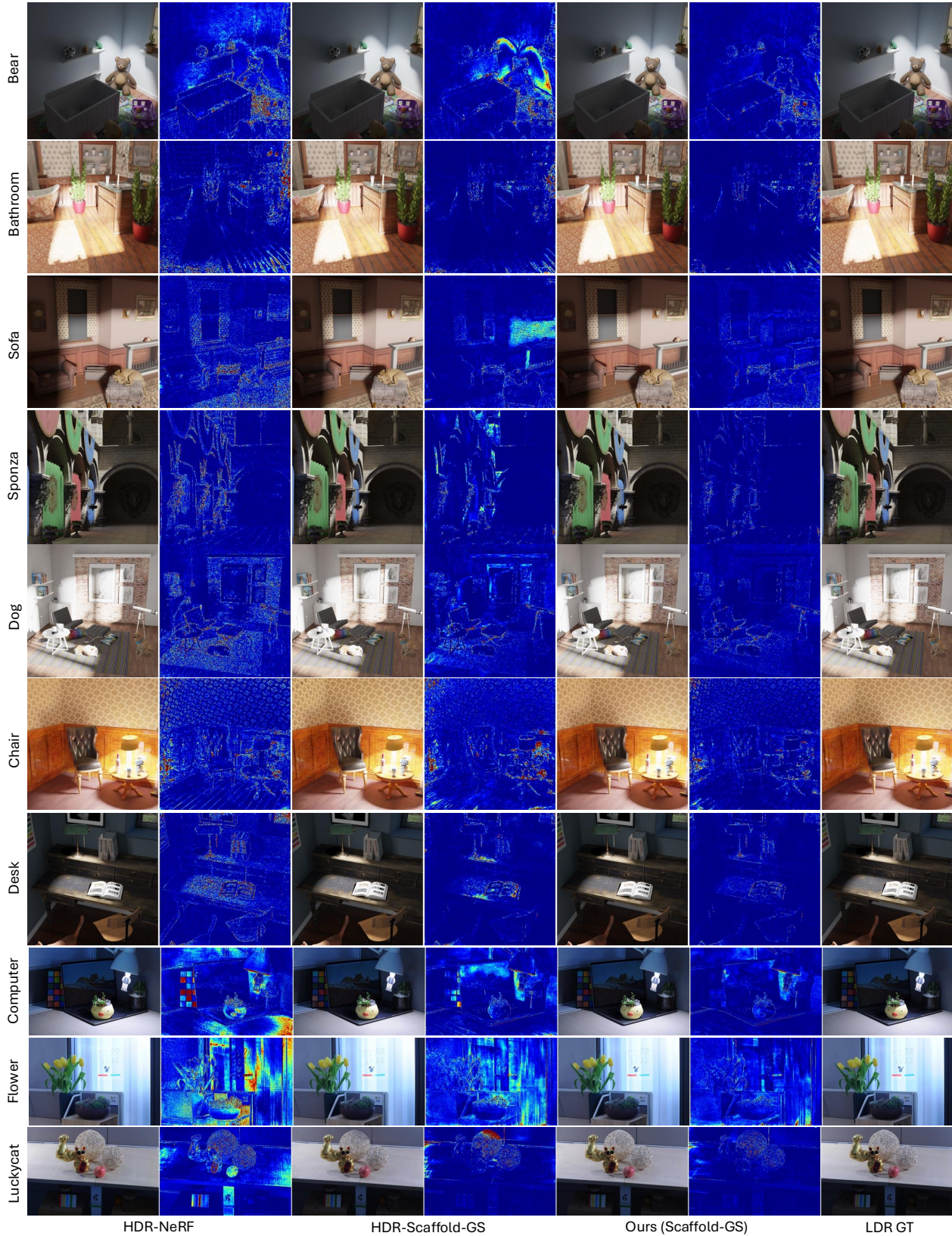


Figure 9. Qualitative LDR comparisons. Error maps in column 2, 4 and 6 show the MSE error compared to the ground truth, where color from blue to red indicates the error from small to large. Our method can reduce LDR fitting errors in some regions.

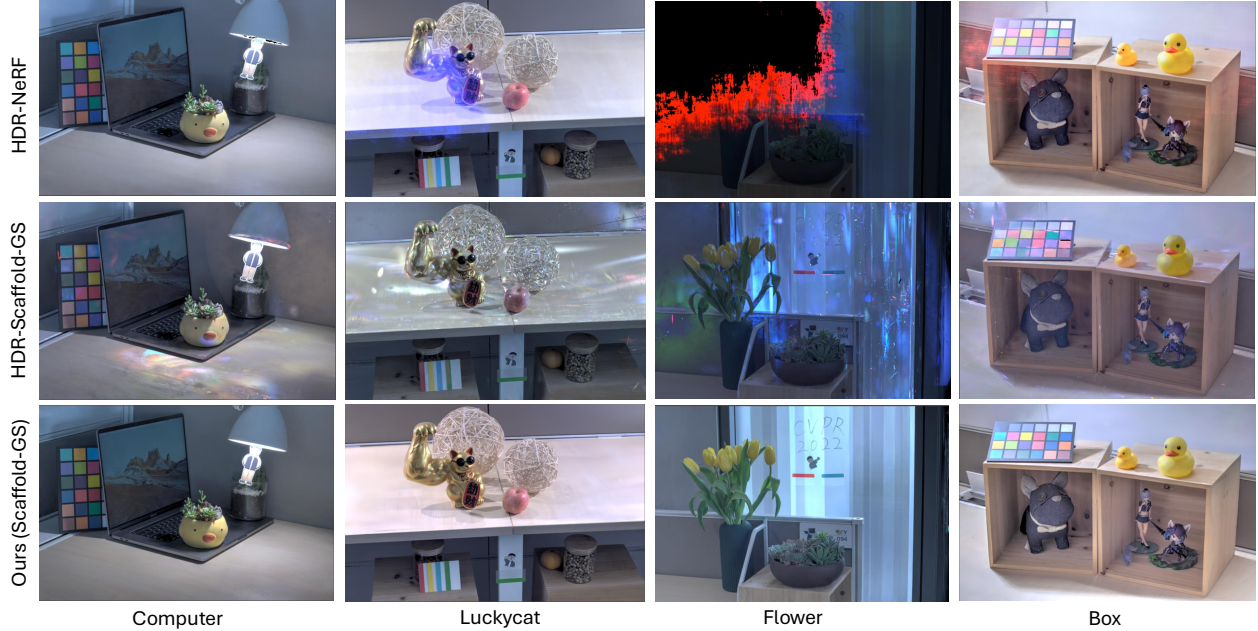


Figure 10. Qualitative HDR comparisons. Our method leads to stable HDR reconstruction results compared to the baselines.

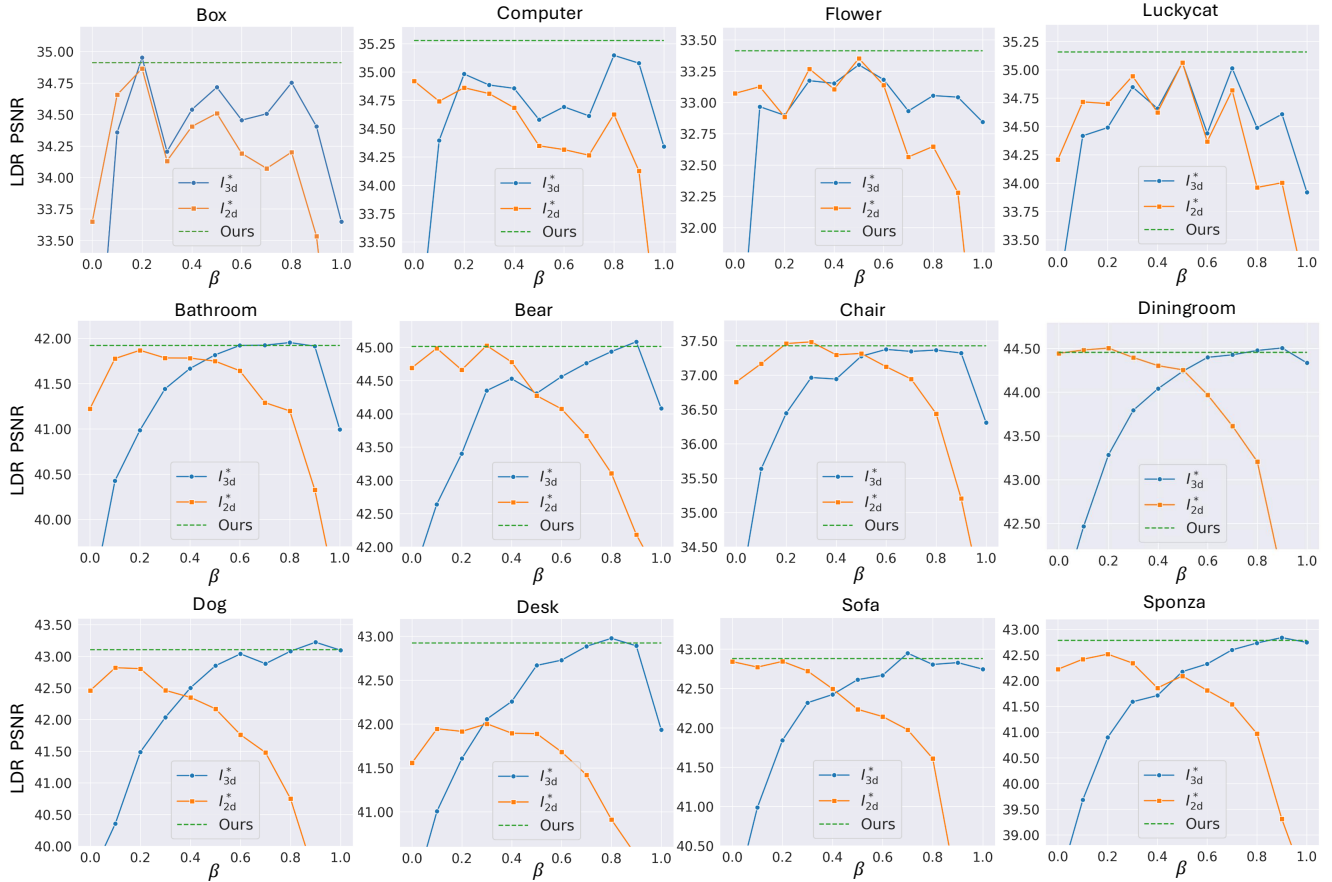


Figure 11. Performance variations of  $I_{3d}^*$  and  $I_{2d}^*$  with respect to  $\beta$  when simply using a loss combination  $\mathcal{L} = \beta\mathcal{L}_{3d} + (1-\beta)\mathcal{L}_{2d}$ . Different scenes exhibit varying optimal values of  $\beta$ . In contrast, our uncertainty-based modulation (green dash line) can robustly achieve optimal results across diverse scenes without the selection of hyper-parameter  $\beta$ . Results include all of HDR-NeRF [18] real and synthetic scenes.